Research Article

Bandgap narrowing and polarization enhancement in (K,Na,Li)(Nb,Sb,Ta)O$_3$+x% Fe$_2$O$_3$ lead-free ceramics for photovoltaic applications

Jian Chen[a], Jiaxing Mao[a], Zihui Wang[a], Yanhui Dong[a], Jinming Guo[a], Mingkai Li[a], Yi Zhang[b], Yinmei Lu[a,*], Yunbin He[a,*]

[a]*Key Laboratory of Green Preparation and Application for Functional Materials, Ministry of Education, Hubei Key Lab of Ferro & Piezoelectric Materials and Devices, Hubei Key Laboratory of Polymer Materials, School of Materials Science and Engineering, Hubei University, Wuhan 430062, China*
[b]*Institute of Photoelectronic Thin Film Devices and Technology, Tianjin Key Laboratory of Thin Film Devices and Technology, Nankai University, Tianjin 300350, China*

Abstract: The need for ferroelectric materials with both narrow bandgaps (E_g) and large remanent polarization (P_r) remains a key challenge to the development of high-efficiency ferroelectric photovoltaic (FPV) devices. In this work, $[(K_{0.43}Na_{0.57})_{0.94}Li_{0.06}][(Nb_{0.94}Sb_{0.06})_{0.95}Ta_{0.05}]O_3$ (KNLNST)-based lead-free ceramics with narrow E_g and large P_r are obtained via Fe$_2$O$_3$ doping. By optimizing the level of Fe$_2$O$_3$ doping, a KNLNST+1.3% Fe$_2$O$_3$ ceramic is fabricated that simultaneously possesses a narrow E_g of 1.74 eV and a large P_r of 27.05 μC/cm^2. These values are much superior to those of undoped KNLNST ceramics (E_g = 3.1 eV and P_r = 17.73 μC/cm^2). While the large P_r stems from the increment of the volume ratio between the orthorhombic and tetragonal phases (V_O/V_T) in KNLNST ceramics by proper amount of Fe^{3+} doping, the narrow E_g is attributed to the coupling interaction between the Fe^{3+} dopants and the B-site Sb^{3+} host ions. Moreover, a switchable photovoltaic effect caused by the ferroelectric depolarization electric field (E_{dp}) is observed in the KNLNST+1.3% Fe$_2$O$_3$ ceramic-based device. Thanks to the narrower E_g and larger P_r of the doped ceramic, the photovoltaic performance of the corresponding device (open-circuit voltage (V_{oc}) = −5.28 V and short-circuit current density (J_{sc}) = 0.051 μA/cm^2) under a downward poling state is significantly superior to that of an undoped KNLNST-based device (V_{oc} = −0.46 V and J_{sc} = 0.039 μA/cm^2). This work offers a feasible approach to developing ferroelectric materials with narrow bandgaps and large P_r for photovoltaic applications.

Keywords: ferroelectrics; bandgap (E_g); remanent polarization (P_r); photovoltaic effect; $[(K_{0.43}Na_{0.57})_{0.94}Li_{0.06}][(Nb_{0.94}Sb_{0.06})_{0.95}Ta_{0.05}]O_3$ (KNLNST)

* Corresponding authors.

E-mail: Y. Lu, yinmei_lu@hubu.edu.cn;

     Y. He, ybhe@hubu.edu.cn

1 Introduction

Ferroelectric materials have attracted enormous attention in the field of solar cells since the bulk photovoltaic effect was discovered in 1956 [1–3]. The bulk photovoltaic effect is associated with the spontaneous polarization induced by the inversion symmetry breaking of ferroelectric materials and is different from the working mechanism of traditional p–n junction solar cells [4]. In traditional p–n junction solar cells, the photogenerated carriers are separated by the built-in electric field at the p–n junction interface. As a result, the open-circuit voltage (V_{oc}) of these solar cells is lower than the bandgap (E_g) of the light-absorbing layer material, leading to a limited power conversion efficiency (PCE) of the solar cells that cannot exceed the Shockley–Queisser limit (33.7%) [5,6]. In contrast, the driving force of photogenerated carriers in ferroelectric photovoltaic (FPV) devices is caused by a polarization-induced electric field throughout the materials. Thus, an FPV device shows an anomalous photovoltaic effect with an over-bandgap V_{oc}, which makes it possible for such devices to break the Shockley–Queisser PCE limit [7]. Moreover, the photovoltaic performance of these devices can be modulated by external poling electric fields [6,8]. These features have made ferroelectric-based photovoltaic devices an ideal alternative and/or complement to traditional p–n junction solar cells. However, most ferroelectric materials, such as $K_{0.5}Na_{0.5}NbO_3$ (KNN; E_g = 3.2 eV) [9], $PbZr_{0.65}Ti_{0.35}O_3$ (E_g = 3.4 eV) [10], and $BaTiO_3$ (BTO; E_g = 3.2 eV) [11], possess wide bandgaps of above 3.0 eV, which result in the insufficient absorption of sunlight. Therefore, most reported FPV devices exhibit very low PCE values of below 1% [12,13].

Huge efforts have been made to decrease the bandgaps of ferroelectric materials via appropriate ion doping to improve their absorption of sunlight. $(1-x)KNbO_3-xBa(Ni_{1/2}Nb_{1/2})O_{3-\delta}$ (KBNNO) ceramics with direct narrow bandgaps of around 1.39 eV were first fabricated in 2013 by Grinberg *et al.* [14] by introducing $BaNi_{1/2}Nb_{1/2}O_{3-\delta}$ to KNN, which was further explored by other researchers [5,15]. A $Bi_2(Fe,Cr)O_6$ ferroelectric thin film with an E_g of 1.4 eV and a room-temperature remanent polarization (P_r) of 5 μC/cm² was achieved in 2015 [16], with the corresponding photovoltaic device showing a high PCE of 8.1% under 1 sun illumination. Unfortunately,

narrowing the bandgaps of ferroelectric materials usually causes deterioration in the ferroelectricity (i.e., a decrease in P_r), which is unfavorable to the separation of photogenerated carriers. Hence, the development of ferroelectric materials with both large P_r and narrow E_g is an urgent priority. Consequently, several new ferroelectric materials including $Bi_{0.98}Ca_{0.02}Fe_{0.95}Mn_{0.05}O_3$ (E_g = 2.41 eV and P_r = 92.5 μC/cm²) [12], $0.8KNbO_3-0.2SrFeO_{3-\delta}$ (E_g ≈ 2.18 eV and P_r ≈ 2.5 μC/cm²) [17], and $PbTiO_3-BiFeO_3-Bi(Ni_{1/2}Ti_{1/2})O_3$ (PT–BF–BNT; E_g = 2.25 eV and P_r =32 μC/cm²) [18] with narrow E_g and large P_r have recently been developed. However, the bandgaps of these reported ferroelectric materials are still above 2.0 eV, which is not beneficial to the absorption of visible light.

Among ferroelectric materials, KNN-based ceramics have aroused significant attention because of their excellent thermal stability, piezoelectric properties, and non-toxicity [19]. In particular, (Li,Sb,Ta)-doped KNN ceramics have been widely investigated since Saito *et al.* [19] reported $(Na_{0.52}K_{0.44}Li_{0.04})(Nb_{0.86}Ta_{0.10}Sb_{0.04})O_3$ ceramics with a high piezoelectric constant (d_{33}) that is comparable to those of lead-based ceramics. In Ref. [20], it was found that the ferroelectricity of $[(K_{0.43}Na_{0.57})_{0.94}Li_{0.06}][(Nb_{0.94}Sb_{0.06})_{0.95}Ta_{0.05}]O_3$ (KNLNST) ceramics was significantly improved by Fe^{3+} doping. Moreover, it was recently reported that the doping of transition metal ions (Fe^{3+}, Co^{3+}, and Ni^{3+}) effectively reduced the bandgaps of ferroelectric materials by introducing abundant energy levels within the bandgap [21]. It is therefore feasible to simultaneously decrease the E_g and improve the P_r of KNLNST-based ceramics by incorporating Fe_2O_3.

In this work, we introduce Fe_2O_3 into a lead-free ferroelectric KNLNST ceramic in an optimal quantity according to Refs. [20,22–24]. It is found that Fe_2O_3 doping can simultaneously decrease the E_g and enhance the P_r of the KNLNST-based ceramics effectively. In particular, the KNLNST+1.3% Fe_2O_3 ceramic shows a narrow E_g of 1.74 eV and a large P_r of 27.05 μC/cm², which are superior to those of the previously reported ferroelectric materials. Moreover, the KNLNST+1.3% Fe_2O_3 ceramic-based photovoltaic device shows a switchable photovoltaic effect under various poling states, with a V_{oc} of −5.28 V and a short-circuit current density (J_{sc}) of 0.051 μA/cm² under a downward poling state. These values are significantly superior to those of the undoped KNLNST-based device (V_{oc} = −0.46 V and J_{sc} = 0.039 μA/cm²).

2 Materials and methods

In this work, KNLNST+x% Fe_2O_3 (Fe_2O_3 doping amount (x) = 0–2.2) lead-free ceramics were prepared by using the conventional solid state method, and the raw materials were Na_2CO_3 (99.8%), K_2CO_3 (99%), Li_2CO_3 (99.99%), Nb_2O_5 (99.99%), Ta_2O_5 (99.5%), Sb_2O_3 (99.99%), and Fe_2O_3 (99%). The detailed synthesis procedure was described in Ref. [20]. All the disks were sintered in air at 1100 ℃ for 5 h in a 10-mL enclosed alumina copple by adding powders of the same chemical composition as the assisting sintering atmosphere. Both surfaces of the polished 0.2-mm-thick ceramic disks were coated with a silver (Ag) paste for the electrical measurements. For the fabrication of relevant FPV devices, the 0.2-mm-thick ceramic disks were further polished to 30 μm, and transparent indium tin oxide (ITO) square electrodes (500 μm × 500 μm) were prepared by pulsed laser deposition (PLD) on one surface of the ceramics as top electrodes while keeping the other-side Ag pastes as bottom electrodes to form ITO/KNLNST+x% Fe_2O_3/Ag devices.

The crystal structures of the sintered ceramic disks were determined by the X-ray diffractometer (D8 Advance, Bruker, Germany) with Cu Kα radiation (λ = 1.54184 Å). The morphologies and elemental mappings of the ceramics were characterized by a field emission scanning electron microscope (FE-SEM; Sigma 500, Zeiss, Germany) and an attached energy dispersive spectrometer (X-flash 6/30, Bruker, Germany), respectively. The temperature (T)-dependent dielectric properties of the ceramics were measured by an impedance analyzer (WK6500B, Wayne Kerr Electronics, UK) at 10 kHz. The elemental analyses of the ceramics were performed by an X-ray photoelectron spectrometer (Escalab 250Xi, Thermo Scientific, USA) with an Al Kα source (the photon energy ($h\nu$) = 1486.6 eV, where h is the Planck constant, and ν is the frequency). The room-temperature polarization–electric field (P–E) hysteresis loops were recorded at 100 Hz by a ferroelectric analyzer (Precision LC II, Radiant Technologies Inc., USA) with a high-voltage power supply. To prevent the electrical breakdown of air during ferroelectric testing, the samples were immersed in silicone oil for the P–E measurements. The diffuse reflectance spectra of the ceramic disks were recorded by an ultraviolet–visible– near infrared (UV–Vis–NIR) spectrophotometer (UV-3600 Plus, Shimadzu, Japan) equipped with an integrating sphere attachment (ISR-603). The photocurrent response properties at different wavelengths were measured at room temperature with a photoelectric testing system including a 150-W xenon lamp, a monochromator (Onim-λ3027i, Zolix, China), and a source meter (2635B, Keithley, USA). The current density–voltage (J–V) and current–time (I–t) characteristics were measured by the source meter (2635B, Keithley, USA) under the illumination of a 500 W xenon lamp, which was used to simulate the solar spectrum of AM 1.5 G (100 mW/cm^2).

3 Results and discussion

Figure 1(a) shows the room-temperature X-ray diffraction (XRD) patterns of the KNLNST+x% Fe_2O_3 ceramics with x = 0, 0.25, 0.7, 0.8, 1.0, 1.3, 1.6, 1.9, and 2.2 in the range of 2θ = 20°–60°. All diffraction peaks in the XRD patterns can be indexed straightforwardly according to JCPDS No. 32-0822, and no additional peaks are observed in the patterns, indicating that all the KNLNST+x% Fe_2O_3 ceramics have a pure perovskite structure [20,25,26]. Moreover, with the increasing Fe_2O_3 doping content, the (220)/(002) diffraction peaks of the KNLNST+x% Fe_2O_3 ceramics shift toward higher angles when x < 1.0, but then shift toward lower angles as the doping content increases further (Fig. 1(b)). These results indicate that the lattice constants of the KNLNST+x% Fe_2O_3 ceramics show a "V"-type variation trend with the increasing Fe_2O_3 doping content, which is attributed to the substitution of A-site (K^+/Na^+) or B-site (Nb^{5+}) cations of KNLNST by Fe^{3+}. There are abundant A-site vacancies occurred in KNLNST+ x% Fe_2O_3 ceramics resulting from the volatilization of K^+/Na^+ ions during the high-temperature sintering process, and thus Fe^{3+} is more likely to occupy A-site K^+/Na^+ vacancies for low levels of Fe_2O_3 doping (x < 1.0) but tends to replace B-site Nb^{5+} when x > 1.0. As the ionic radius of Fe^{3+} (0.785 Å) is smaller than that of K^+ (1.38 Å) or Na^+ (1.02 Å) but larger than that of Nb^{5+} (0.64 Å) [27], the evolution of Fe^{3+} substitution from the A site to B site causes the V-type variation of lattice constants, as observed in Fig. 1(b). The (220) and (002) diffraction peaks of the KNLNST+x% Fe_2O_3 were fitted, and a typical example of this Gaussian fitting is presented in Fig. 1(c). The intensity ratio of (220) and (002) peaks ($I_{(220)}/I_{(002)}$) is widely used to
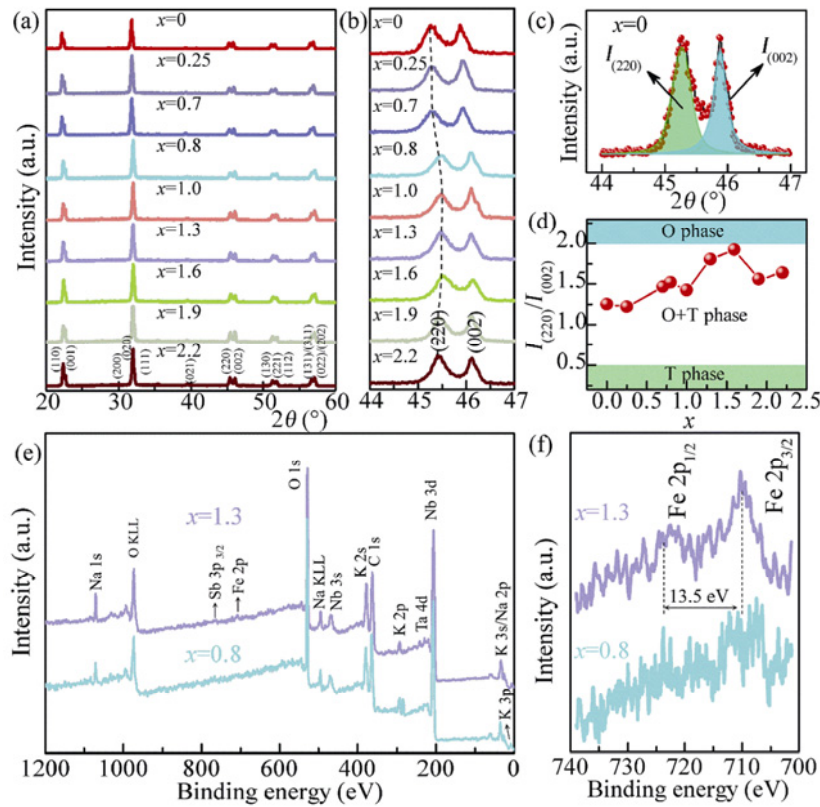
Fig. 1 (a) XRD patterns of KNLNST+x% Fe$_2$O$_3$ ceramics. The diffraction peaks are indexed for the O phase according to JCPDS No. 32-0822. (b) Magnified patterns in the 2θ range of 44°–47°. (c) Gaussian fitting of (220) and (002) diffraction peaks of KNLNST. (d) Calculated $I_{(220)}/I_{(002)}$ ratios of KNLNST+x% Fe$_2$O$_3$ ceramics. (e) XPS survey spectra and (f) high-resolution Fe 2p spectra of KNLNST+x% Fe$_2$O$_3$ ceramics with x = 0.8 and 1.3.

represent the volume ratio between the orthorhombic and tetragonal phases (V_O/V_T) in KNN-based ceramics, as seen in Refs. [20,25]. Figure 1(d) shows the calculated $I_{(220)}/I_{(002)}$ ratio of the KNLNST+x% Fe$_2$O$_3$ ceramics as a function of the Fe$_2$O$_3$ doping content. As clearly seen, the $I_{(220)}/I_{(002)}$ values of the ceramics increase from 1.25 (x = 0) to 1.92 (x = 1.6) at first, and then decrease to 1.64 (x = 2.2), implying that both the orthorhombic (O) and tetragonal (T) phases coexist in the ceramics, and the V_O/V_T reaches a maximum value (most predominance of the O phase) in the KNLNST+ 1.6% Fe$_2$O$_3$ ceramic. Figure 1(e) presents the X-ray photoelectron spectroscopy (XPS) survey spectra of two representative KNLNST+x% Fe$_2$O$_3$ ceramics with x = 0.8 and 1.3. Characteristic peaks of Na, K, Nb, Ta, Sb, Fe, and O are shown in Fig. 1(e), confirming the existence of these elements in the ceramics. No signals from Li are detected by the XPS because of its low content and very low sensitivity factor associated with its small atomic number. In Fig. 1(f), the high-resolution XPS spectra of Fe 2p are displayed for both ceramics. The peak intensities in both spectra vary according to

the Fe doping contents. More importantly, for each spectrum, the peaks located around 710.3 and 723.8 eV are assigned to the Fe 2p$_{3/2}$ and Fe 2p$_{1/2}$, respectively, confirming the presence of Fe^{3+} in the ceramics. This validates our above discussion (cf. Fig. 1(b)) about the evolution of Fe occupation from the A site to B site based on the ionic-size comparison between the hosts of K$^+$/Na$^+$ and Nb^{5+} with the Fe dopant assuming its valence of +3.

The SEM images revealing the surface morphology of the KNLNST+x% Fe$_2$O$_3$ ceramics are displayed in Fig. S1 in the Electronic Supplementary Material (ESM). All the ceramics show a dense microstructure with square-shaped grains, and there is no obvious difference in the grain sizes of these ceramics. The SEM image and corresponding energy dispersive spectroscopy (EDS) elemental mapping images of the representative KNLNST+1.3% Fe$_2$O$_3$ ceramic are shown in Fig. 2. It is seen that each element is uniformly distributed, and no elemental segregation occurs in the ceramic. This indicates that the Fe dopants are well incorporated into the lattice of KNLNST, in
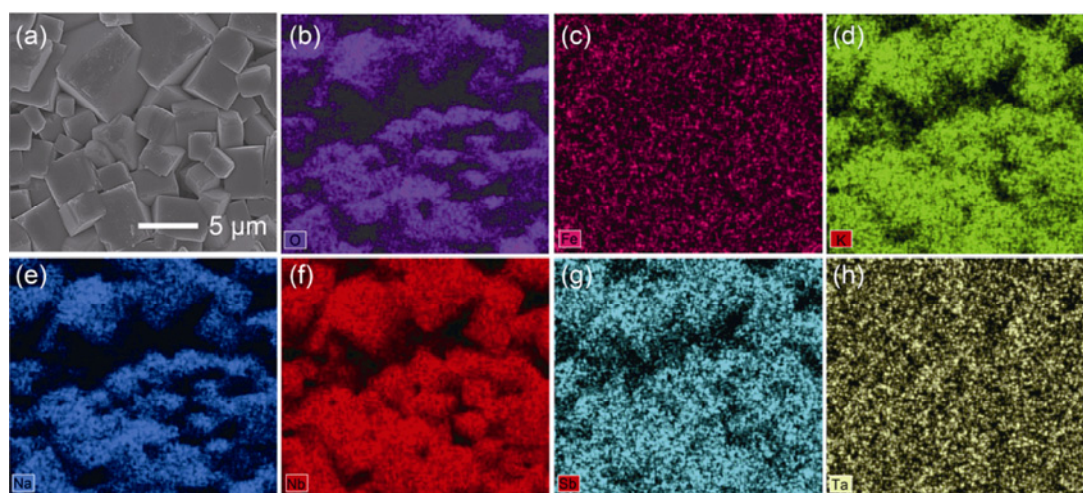
Fig. 2　(a) SEM image and (b–h) corresponding EDS elemental mapping images of KNLNST+1.3% Fe_2O_3 ceramic.

accordance with the above XRD measurements, which reveal no detectable Fe-containing secondary phases in the KNLNST+x% Fe_2O_3 ceramics.

Figure 3(a) presents the T-dependent relative permittivity (ε_r) curves of the KNLNST+x% Fe_2O_3 ceramics recorded between room temperature and 400 ℃. There are two permittivity peaks shown in each curve, which correspond to the orthorhombic–tetragonal (O–T) and tetragonal–cubic (T–C) phase transitions in the ceramics. With the increasing Fe_2O_3 content in the ceramics, both the O–T phase transition temperature ($T_{O–T}$) and the T–C phase transition temperature ($T_{T–C}$) first increase, and then decrease, reaching the maximum values at $x = 1.6$ (Fig. 3(b)). This reveals a phase evolution with varying V_O/V_T in the ceramics that is in accordance with the XRD results, as shown in Fig. 1.
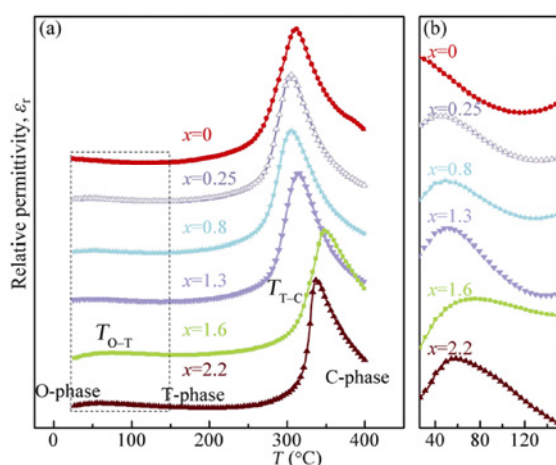

Fig. 3　(a) T-dependent ε_r curves measured at 100 kHz for representative KNLNST+x% Fe_2O_3 ceramics. (b) Enlargement of the dotted box in (a).

Figure 4(a) shows the $P–E$ hysteresis loops of the KNLNST+x% Fe_2O_3 ceramics measured at an electric field of 80 kV/cm. All of the ceramics exhibit saturated hysteresis loops, indicating excellent ferroelectricity. The coercive electric field (E_c) and P_r of the ceramics are extracted from the $P–E$ hysteresis loops, as shown in Fig. 4(b). The varying trend of the P_r is basically consistent with that of the $I_{(220)}/I_{(002)}$ (V_O/V_T) ratios, as shown in Fig. 1(d), which might be attributed to the fact that there are more polarization directions (twelve) in the O-phase than those in the T-phase ceramics (six) [28]. Conversely, with the increasing Fe^{3+} doping content, the E_c of the ceramics first decreases, and then increases with a minimum E_c of 21.79 kV/cm appearing at $x = 1.0$. For $x < 1.0$ samples, the Fe^{3+} dopants with a higher valence occupy the A-site Na^+/K^+ vacancies, as indicated in Fig. 1(b), acting as donors and causing a "soft doping effect" in the ceramics, which results in decreased oxygen vacancies, and thus suppressed domain-wall pinning effect, making the ceramics easier to pole [29]. Hence, the E_c of the ceramics ($x < 1.0$) first decreases with the increasing Fe^{3+} content. As the Fe^{3+} doping content is further increased ($x > 1.0$), the Fe^{3+} starts to substitute the even higher-valence Nb^{5+} at B sites, behaving like an acceptor, and thus causing "hard doping effect" [30], which leads to increased E_c in the samples.

The optical properties of the KNLNST+x% Fe_2O_3 ceramics were investigated by the diffuse reflectance spectroscopy with a UV–Vis–NIR spectrophotometer. The absorption coefficients (α) of the ceramics were obtained according to the Kubelka–Munk (K–M) function: $\alpha/s = F(R) = (1 − R)^2/(2R)$ [15,31], where s

and *R* are the scattering coefficient and reflectance of the ceramics, respectively. Figure 5(a) presents the absorption spectra of the ceramics. An obvious redshift of the absorption edge of the ceramics is observed with the increasing Fe_2O_3 doping content, implying a narrowed bandgap in the ceramics. The E_g of the samples can be estimated by the equation: $(\alpha h v)^2 = A(h v - E_g)$ [12,15], where *A* is a constant. By extrapolating the linear part of the $(F(R)h v)^2$ curve to the *hv*-axis (Fig. 5(b)), the optical bandgap values of the ceramics were obtained. Figure 5(c) shows the E_g values of the ceramics with various Fe_2O_3 doping contents. It is clearly seen that

Fe_2O_3 doping can effectively decrease the bandgap of KNLNST ceramics, resulting in a continuously tunable E_g ranging from 3.1 to 1.71 eV, which endows KNN-based materials high potential for the application in next-generation solar cells. Moreover, the decrease in the bandgap of the KNLNST+*x*% Fe_2O_3 ceramics leads to varying colors of the ceramics from white (*x* = 0) to brown (*x* = 0.8) and finally to deep brown (*x* = 1.6) (the inset of Fig. 5(c)). As the grain sizes of these ceramics are similar (Fig. S1 in the ESM), the bandgap narrowing of the KNLNST+*x*% Fe_2O_3 ceramics has origins other than the grain size effect.
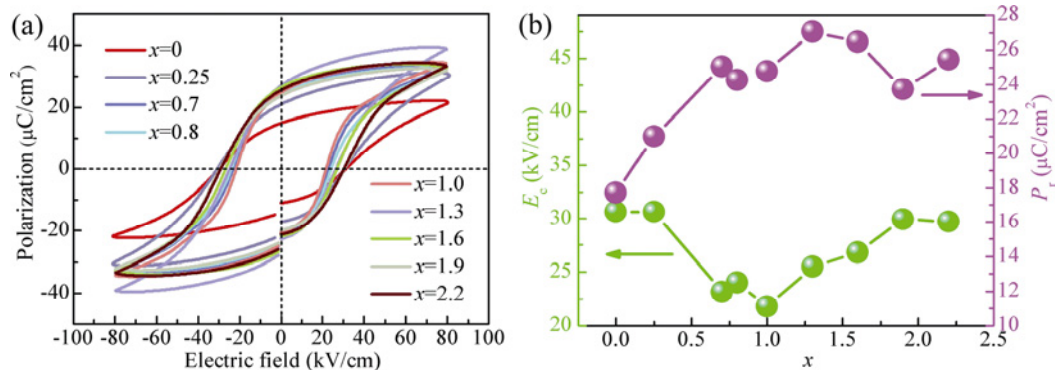

Fig. 4 (a) *P*–*E* hysteresis loops of KNLNST+*x*% Fe_2O_3 ceramics. (b) E_c and P_r as a function of *x*.
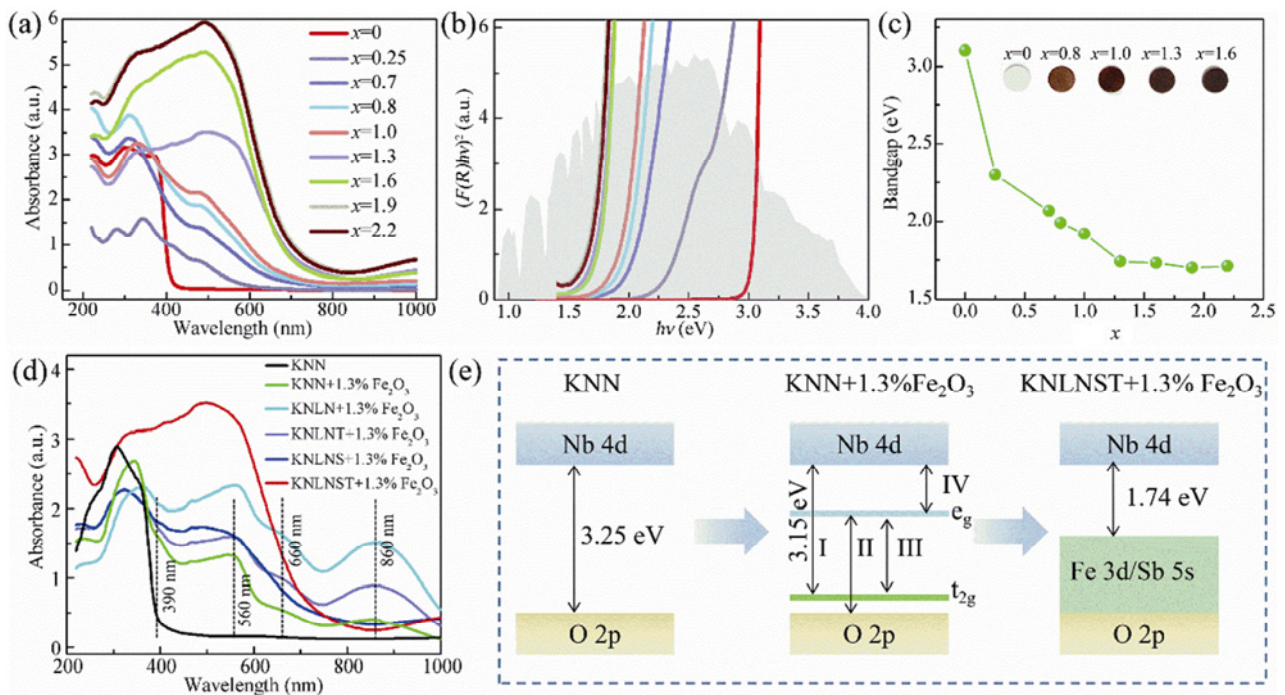

Fig. 5 (a) Optical absorption spectra, (b) $(F(R)h v)^2$–*hv* plots, and (c) optical bandgaps of KNLNST+*x*% Fe_2O_3 ceramics. The inset in (c) shows the KNLNST+*x*% Fe_2O_3 ceramic samples for *x* = 0, 0.8, 1.0, 1.3, and 1.6. (d) Optical absorption spectra of KNN+1.3% Fe_2O_3, $[(K_{0.43}Na_{0.57})_{0.94}Li_{0.06}]NbO_3$ (KNLN)+1.3% Fe_2O_3, $[(K_{0.43}Na_{0.57})_{0.94}Li_{0.06}](Nb_{0.95}Ta_{0.05})O_3$ (KNLNT)+1.3% Fe_2O_3, $[(K_{0.43}Na_{0.57})_{0.94}Li_{0.06}](Nb_{0.95}Sb_{0.05})O_3$ (KNLNS)+1.3% Fe_2O_3, and KNLNST+1.3% Fe_2O_3 ceramics. (e) Energy band diagrams of KNN, KNN+1.3% Fe_2O_3, and KNLNST+1.3% Fe_2O_3 ceramics.

To determine the bandgap narrowing mechanism in the KNLNST+x% Fe_2O_3 ceramics, we further fabricated KNN+1.3% Fe_2O_3, KNLN+1.3% Fe_2O_3, KNLNT+1.3% Fe_2O_3, and KNLNS+1.3% Fe_2O_3 ceramics by using the conventional solid state method and investigated the optical properties of the ceramics. The prepared KNLN+1.3% Fe_2O_3, KNLNT+1.3% Fe_2O_3, and KNLNS+1.3% Fe_2O_3 ceramics show a pure perovskite phase (Fig. S2(a) in the ESM). As shown in Fig. S2(b) in the ESM, the diffraction peaks located at around 45° for the ceramics containing Sb (KNLNS+1.3% Fe_2O_3 and KNLNST+1.3% Fe_2O_3) shift toward higher angles compared with those of the Sb-free ceramics (KNLN+1.3% Fe_2O_3 and KNLNT+1.3% Fe_2O_3), which might be attributed to the higher volume ratio of the O phase in the ceramics containing Sb. Figure 5(d) presents the optical absorption spectra of the KNN+ 1.3% Fe_2O_3, KNLN+1.3% Fe_2O_3, KNLNT+1.3% Fe_2O_3, KNLNS+1.3% Fe_2O_3, and KNLNST+1.3% Fe_2O_3 ceramics. The KNN+1.3% Fe_2O_3, KNLN+1.3% Fe_2O_3, and KNLNT+1.3% Fe_2O_3 Sb-free ceramics show several absorption peaks located at 390, 560, 660, and 860 nm, which is consistent with those reported in Refs. [32,33]. We attribute the optical transitions at wavelengths of 390–900 nm to the splitting of the Fe^{3+} 3d energy level caused by the distortion of the FeO_6 octahedra in the KNN-based materials. Similar optical absorptions have been observed in $(Na_{0.5}Bi_{0.5})TiO_3$–$Ba(Ni_{0.5}Ti_{0.5})O_3$, $(K_{0.48}Na_{0.52})NbO_3$–$(Bi_{0.5}Na_{0.5})(Ni_{0.45}Zr_{0.55})O_3$, and $(Pb_{1-x}La_x)(Zr_{0.65(1-y)}Ti_{0.35(1-y)}Ni_y)O_3$ (x = 0.08, 0.09; y = 0, 0.025) (PLZTN) materials and attributed to Ni^{2+} 3d energy level splitting [9,34,35]. In contrast, the ceramics containing Sb (KNLNS+1.3% Fe_2O_3 and KNLNST+1.3% Fe_2O_3) show only one absorption edge in the visible light region. These results indicate that both Sb^{3+} and Fe^{3+} are the key elements that are responsible for the narrowed bandgap of the KNLNST (KNLNS)+1.3% Fe_2O_3 ceramic. The bandgap of the KNN ceramics is determined to be 3.25 eV (Fig. S3 in the ESM), with the conduction band minimum (CBM) and valence band maximum (VBM) composed mainly Nb 4d and O 2p, respectively (Fig. 5(e)). When Fe_2O_3 is introduced into the KNN, the Fe 3d orbitals interact with the O 2p orbitals, resulting in the narrower bandgap of KNN+1.3% Fe_2O_3 (3.15 eV) [32]. Moreover, the absorption peaks of KNN+1.3% Fe_2O_3 can be well explained by the crystal field theory. The 3d orbitals of Fe^{3+} in the KNN+1.3% Fe_2O_3 ceramic are split into high-energy e_g and low-energy t_{2g} orbitals,

as a result of the Jahn–Teller effect. Thus, the optical absorption peaks of the KNN+1.3% Fe_2O_3 ceramics located at 390, 560, 660, and 860 nm may be ascribed to the electron transitions of t_{2g} → Nb 4d (I), O 2p → e_g (II), t_{2g} → e_g (III), and e_g → Nb 4d (IV), respectively (Fig. 5(e)). In particular, the narrow bandgap of the KNN+1.3% Fe_2O_3 ceramic is attributed to the high-energy shift of the VBM caused by the interaction of t_{2g} orbitals split by Fe 3d orbitals with O 2p orbitals. The Sb and Fe co-doped KNN-based ceramic (KNLNST+1.3% Fe_2O_3) has an even narrower bandgap of 1.74 eV, which might be attributed to the interaction of both e_g and t_{2g} orbitals split by Fe 3d orbitals with Sb 5s orbitals. Xiao *et al*. [36] proposed a similar strategy for achieving narrow-bandgap $Na_{0.5}Bi_{0.5}TiO_3$–BTO-based ferroelectric material without introducing gap states; by N^{3-} and Ni^{2+} co-doping, they obtained $0.95Na_{0.5}Bi_{0.5}TiO_3$–$0.05Ba(Ti_{0.5}Ni_{0.5})(O_xN_{1-x})$ ceramic powders with a much reduced bandgap (from 3.2 to 2.06 eV) and a single absorption edge in the optical absorption spectrum.

The KNLNST+x% Fe_2O_3 ceramic with x = 1.3 possesses the highest P_r (27.05 μC/cm^2) and relatively narrow E_g (1.74 eV) compared to the other prepared samples. In Fig. 6, we further compare the E_g and P_r of the KNLNST+1.3% Fe_2O_3 ceramics fabricated in our work with those of the ferroelectric materials reported in the literature [6,9,14,16–18,34,35,37–56]. The detailed data for these materials are summarized in Table 1. Obviously, the P_r of a ferroelectric material is highly correlated with its E_g, showing a decreasing trend as E_g decreases. Moreover, most ferroelectric materials have bandgaps above 2.0 eV (significantly larger than the ideal bandgap of ~1.4 eV for a photo-absorption layer material), making them inappropriate for the application in solar cells. Unfortunately, ferroelectric materials with bandgaps below 2.0 eV usually have relatively low P_r values. Representative narrow-bandgap ferroelectric materials such as $BiFe_{0.5}Cr_{0.5}O_3$ (BFCO) (1.4 eV) and $BiMnO_3$ (BMO) (1.3 eV) have very small P_r values of 5 and 6.6 μC/cm^2, respectively (Table 1) [16,37]. It is known that a high P_r induces a strong ferroelectric depolarization electric field (E_{dp}) in a ferroelectric material, which favors the separation of photogenerated carriers in FPV devices. Thus, most of the currently reported FPV materials are inappropriate for solar cell applications because of their relatively small P_r but large E_g values. The KNLNST+1.3% Fe_2O_3 ceramic prepared in this
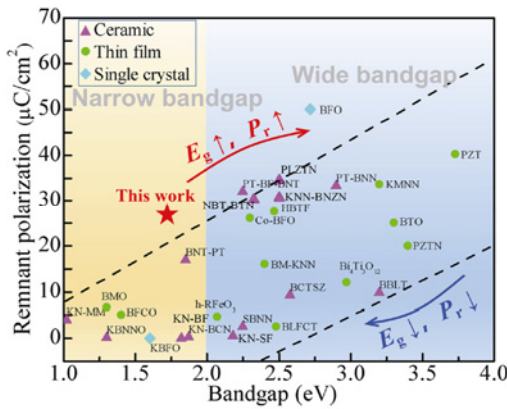
Fig. 6 Comparison of E_g and P_r values of KNLNST+ 1.3% Fe_2O_3 ceramics prepared in this work with those reported in the literature.

work has a narrow E_g of 1.74 eV and a high P_r of 27.05 μC/cm^2. These values are significantly superior to those of the previously reported FPV materials, and thus the KNLNST+1.3% Fe_2O_3 ceramic is a promising material for the application in solar energy harvesting.

As the KNLNST+1.3% Fe_2O_3 ceramic exhibits the highest P_r and relatively narrow E_g, we now further investigate the photovoltaic effect of this sample. Figure 7(a) shows a structural diagram of a KNLNST+ 1.3% Fe_2O_3 ceramic-based device for photovoltaic measurements. Before each measurement, the ceramics were poled by applying a 220 V positive bias voltage to the top ITO electrode of the device for 6 min (denoted as the downward poling state). The *J–V*

Table 1 Data on ferroelectric materials studied for photovoltaic applications in Refs. [6,9,14,16–18,34,35,37–56]

| Material	E_g (eV)	P_r (μC/cm^2)	Preparation method	Thin film or bulk	Ref.
$Bi(Ni_{2/3}Ta_{1/3})O_3$–$PbTiO_3$ (BNT–PT)	1.85	17	Solid state method	Ceramics	[6]
$(1-x)(K_{0.48}Na_{0.52})NbO_3$–$x(Bi_{0.5}Na_{0.5})(Zr_{0.55}Ni_{0.45})O_{3-\delta}$ (KNN–BNZN)	~2.5	30.7	Solid state method	Ceramics	[9]
KBNNO	1.1–3.8	0–5 (at 77 K)	Solid state method	Ceramics	[14]
BFCO	1.4	5	PLD	Thin film	[16]
$KNbO_3$–$SrFeO_{3-\delta}$ (KN–SF)	2.18	< 0.5	Solid state method	Ceramics	[17]
PT–BF–BNT	2.25–2.8	32–39	Solid state method	Ceramics	[18]
$0.05Na_{0.5}Bi_{0.5}TiO_3$–$0.05Ba(Ti_{0.5}Ni_{0.5})O_{3-\delta}$ (NBT–BTN)	~2.3	31.2	Solid state method	Ceramics	[34]
PLZTN	2.5	34.4	Solid state method	Ceramics	[35]
BMO	1.3	6.6	PLD	Thin film	[37]
BTO	3.3	25	PLD	Thin film	[38]
$BiFeO_3$ (BFO)	2.72	50	—	Single crystal	[39]
$Bi_4Ti_3O_{12}$	2.97	12.04	Sol–gel	Thin film	[40]
$(1-x)KNbO_3$–$xBaCo_{1/3}Nb_{2/3}O_3$ (KN–BCN)	1.87–3.26	0.31–2.14	Solid state method	Ceramics	[41]
$Ba_{1-x}(Bi_{0.5}Li_{0.5})_xTiO_3$ (BBLT)	3.2	9.75	Solid state method	Ceramics	[42]
$BiFe_{1-x}Co_xO_3$ (Co–BFO)	2.3–2.7	26.1–60	Sol–gel	Thin film	[43]
$BiMnO_3$–$K_{0.5}Na_{0.5}NbO_3$ (BM–KNN)	2.4	~16	Sol–gel	Thin film	[44]
$Pb(Zr_{0.52}Ti_{0.48})O_3$ (PZT)	3.73	40.3	Sol–gel	Thin film	[45]
h-$RFeO_3$	2.07	4.7	Radio frequency (RF) magnetron sputtering	Thin film	[46]
$Sr_{0.91}Bi_{2.09}Nb_{1.91}Ni_{0.09}O_{8.91}$ (SBNN)	2.25	2.5	Solid state method	Ceramics	[47]
$KBiFe_2O_5$ (KBFO)	1.6	< 0.05	—	Single crystal	[48]
KNN–Mn (KMNN)	3.2	33.6	Sol–gel	Thin film	[49]
$Pb(Zr_{0.2}Ti_{0.8})_{0.70}Ni_{0.30}O_{3-\delta}$ (PZTN)	3.4–4.0	13–20	PLD	Thin film	[50]
Holmium-doped $Bi_5Ti_3FeO_{15}$ (HBTF)	2.47	27.6	Chemical solution deposition	Thin film	[51]
$Bi_{3.25}La_{0.75}Fe_{0.25}Co_{0.75}Ti_2O_{12}$ (BLFCT)	2.48	2.6	PLD	Thin film	[52]
$PbTiO_3$–$Bi(Ni_{2/3+x}Nb_{1/3-x})O_{3-\delta}$ (PT–BNN)	2.9–3.0	33	Solid state method	Ceramics	[53]
$(Ba,Ca)(Ti,Sn,Zr)O_3$ (BCTSZ)	2.58	9.25	Solid state method	Ceramics	[54]
$(1-x)KNbO_3$–$xMgMnO_{3-\delta}$ (KN–MM)	1.02	4	Solid state method	Ceramics	[55]
$KNbO_3$–$BaFeO_{3-\delta}$ (KN–BF)	1.82	0	Solid state method	Ceramics	[56]
KNLNST+1.3% Fe_2O_3	**1.74**	**27.05**	**Solid state method**	**Ceramics**	**This work**
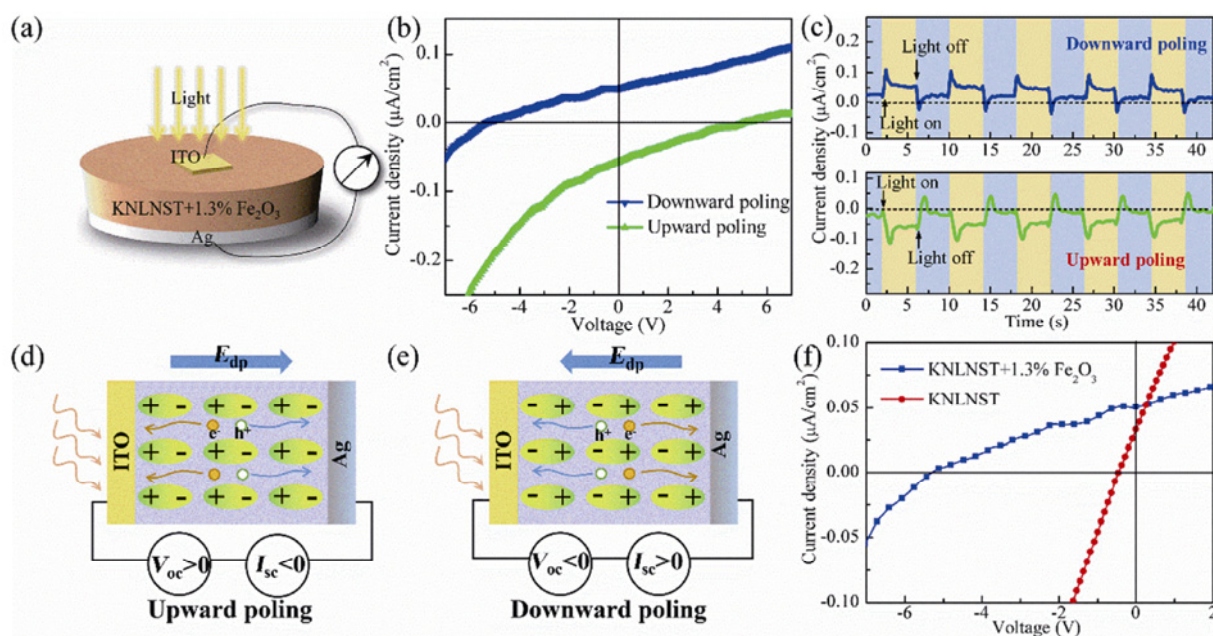
Fig. 7 (a) Structural diagram of KNLNST+1.3% Fe_2O_3 ceramic-based photovoltaic device. (b) *J–V* characteristics and (c) photocurrent responses of KNLNST+1.3% Fe_2O_3 ceramic-based device in upward and downward poling states under AM 1.5 G illumination. Diagrams of separation process of photogenerated carriers of device under (d) upward poling state and (e) downward poling state. Note: e^- and h^+ mean the electrons and holes, respectively. (f) Comparison of photovoltaic performance of KNLNST+1.3% Fe_2O_3 and KNLNST ceramic-based devices.

curves for the KNLNST+1.3% Fe_2O_3 ceramic-based device under the upward and downward poling states under AM 1.5 G illumination are shown in Fig. 7(b). The device shows a clearly switchable photovoltaic effect. The V_{oc} and J_{sc} of the device under an upward poling state are 5.27 V and −0.057 μA/cm², respectively, while totally reversed values of V_{oc} (−5.28 V) and J_{sc} (0.051 μA/cm²) are observed for the device under a downward poling state. The above-bandgap V_{oc} of the device is consistent with those reported in Refs. [18,53] involving ferroelectric ceramics. It is noted that the J_{sc} of the device is rather small, which is ascribed to the low conductivity of the ceramics. Figure 7(c) shows the steady photocurrent responses at zero bias for the device under various poling states. It is clear that the photocurrents (I_{ph}) of the device under upward and downward poling states are consistent with the J_{sc} values (Fig. 7(b)), which further confirms the *J–V* measurements. The switching of the V_{oc} and J_{sc} observed in the KNLNST+1.3% Fe_2O_3 ceramic-based device can be attributed to the switching of the ferroelectric polarization caused by the external poling electric field. For the KNLNST+1.3% Fe_2O_3 ceramic under an upward poling state, an E_{dp} with a direction pointing from the top ITO electrode to the bottom Ag electrode is

induced by the external poling electric field (Fig. 7(d)). Meanwhile, a reverse E_{dp} of the same magnitude with its direction pointing from the bottom Ag electrode to the top ITO electrode is generated in the ceramic when the device is under a downward poling state (Fig. 7(e)). Thus, the V_{oc} and J_{sc} for the device under various poling states are of the same magnitude but in reversed directions (polarities). We further compare the photovoltaic performance of the KNLNST+1.3% Fe_2O_3 ceramic with the Fe-free KNLNST ceramics (Fig. 7(f)). The V_{oc} (−5.28 V, corresponding to a photogenerated electric field (E_p) of 1.76 kV/cm) and J_{sc} (0.051 μA/cm²) of the KNLNST+1.3% Fe_2O_3 ceramic-based device are obviously superior to those of the KNLNST-based device (V_{oc} = −0.46 V and J_{sc} = 0.039 μA/cm²). Moreover, the photovoltaic performance of the KNLNST+1.3% Fe_2O_3 ceramic-based device is comparable to those of the previously reported ferroelectric ceramics, due to its large P_r and narrow E_g. For example, the E_p of the BBLT (P_r = 9.75 μC/cm²) [42], KBNNO (P_r = 5 μC/cm²) [14], and PT–BF–BNT ceramics (P_r = 32 μC/cm²) [18] are 0.32, 1.4, and 1.7 kV/cm, respectively, which are inferior to that of our device.

As shown in Fig. 8(a), the photocurrent responses of the KNLNST+1.3% Fe_2O_3 ceramic under light illumination of various wavelengths were investigated.
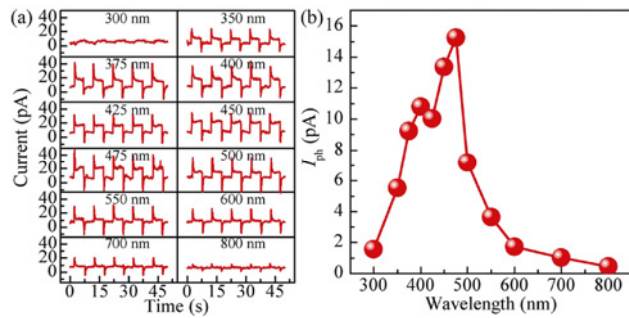
Fig. 8 (a) Photocurrent responses of KNLNST+1.3% Fe_2O_3 ceramic under illumination with incident light of various wavelengths. (b) I_{ph} as a function of incident light wavelength.

The KNLNST+1.3% Fe_2O_3 ceramic shows a steady and reproducible photocurrent response to UV light and visible light, spanning a spectral range of 350–700 nm. It exhibits two photocurrent response peaks at 400 and 475 nm (Fig. 8(b)). These results further verify the narrow bandgap of the KNLNST+1.3% Fe_2O_3 ceramic, which is consistent with the results of the optical absorption spectra (Fig. 5(a)). In comparison, the photocurrent response of the KNLNST ceramic without Fe doping is too weak to be detected under zero bias because the weak E_{dp} in the KNLNST ceramic is unable to separate photogenerated carriers efficiently. Thus, a positive bias of 1 V was applied to the top electrode of the KNLSNT device to separate the photogenerated carriers produced in the KNLSNT ceramic. An evident photocurrent response to UV light is observed (Fig. S4 in the ESM), which is correlated with the band edge transition of e^-. No obvious photocurrent response can be observed in the visible light range because the hv is too low to trigger the band edge transition in the KNLNST with a bandgap of 3.1 eV. Thus, the superior device performance of the KNLNST+1.3% Fe_2O_3 ceramic-based device can be ascribed to the following factors. (i) The narrower bandgap of the KNLNST+1.3% Fe_2O_3 ceramic leads to more photogenerated carriers being produced in the KNLNST+1.3% Fe_2O_3 ceramic-based device than those in the KNLNST-based device. (ii) The larger P_r in the KNLNST+1.3% Fe_2O_3 ceramic results in a larger E_{dp} in the device, which is favorable to the separation and transport of photogenerated carriers.

4   Conclusions

In this work, a series of lead-free KNLNST+x% Fe_2O_3 ceramics (x = 0–2.2) with a pure perovskite phase structure were fabricated by using the traditional solid state method. The XRD results suggest that the ferroelectric O and T phases coexist in these ceramics. The V_O/V_T ratio of the ceramics first increases, and then decreases. The P_r of the ceramics shows a similar variation trend to the V_O/V_T ratios, and reaches a maximum value of 27.03 μC/cm^2 at x = 1.3, which is attributed to the fact that O-phase KNN-based ceramics have more polarization directions (twelve) than T-phase ones (six). The bandgap of the KNLNST+x% Fe_2O_3 can be continuously modulated from 3.1 eV (x = 0) to 1.71 eV (x = 2.2) by increasing the Fe_2O_3 doping content, which is originated from the co-doping of Fe^{3+} and Sb^{3+}. The KNLNST+1.3% Fe_2O_3 ceramic simultaneously possesses the highest P_r (27.03 μC/cm^2) and relatively narrow E_g (1.74 eV) among the samples. The KNLNST+ 1.3% Fe_2O_3 ceramic-based photovoltaic device shows a switchable photovoltaic behavior due to the polarization flipping in the ceramic caused by the external poling electric fields. An above-bandgap V_{oc} of −5.28 V and J_{sc} of 0.051 μA/cm^2 were observed in the downward-poled KNLNST+1.3% Fe_2O_3 ceramic-based photovoltaic device. These values are much superior to those of a photovoltaic device based on KNLNST without Fe doping. This improvement in the photovoltaic performance can be attributed to the narrower E_g and higher P_r of the KNLNST+1.3% Fe_2O_3 ceramic. The lead-free KNN-based ferroelectric material with a narrow bandgap and large P_r developed in this work has broad application prospects in solar cells.

Declaration of competing interest

清华大学出版社 | SciOpen
Tsinghua University Press

Electronic Supplementary Material

Supplementary material is available in the online version of this article at https://doi.org/10.26599/JAC.2023.9220763.

References

[1] Von der Linde D, Glass AM, Rodgers KF. Multiphoton photorefractive processes for optical storage in $LiNbO_3$. *Appl Phys Lett* 1974, **25**: 155–157.

[2] Koch WTH, Munser R, Ruppel W, *et al*. Bulk photovoltaic effect in $BaTiO_3$. *Solid State Commun* 1975, **17**: 847–850.

[3] Chynoweth AG. Surface space-charge layers in barium titanate. *Phys Rev* 1956, **102**: 705–714.

[4] Chakrabartty J, Harnagea C, Celikin M, *et al*. Improved photovoltaic performance from inorganic perovskite oxide thin films with mixed crystal phases. *Nat Photonics* 2018, **12**: 271–276.

[5] Zhang QF, Xu F, Xu MJ, *et al*. Lead-free perovskite ferroelectric thin films with narrow direct band gap suitable for solar cell applications. *Mater Res Bull* 2017, **95**: 56–60.

[6] Pang DF, Liu XT, He X, *et al*. Anomalous photovoltaic effect in $Bi(Ni_{2/3}Ta_{1/3})O_3$–$PbTiO_3$ ferroelectric solid solutions. *J Am Ceram Soc* 2019, **102**: 3448–3456.

[7] Spanier JE, Fridkin VM, Rappe AM, *et al*. Power conversion efficiency exceeding the Shockley–Queisser limit in a ferroelectric insulator. *Nat Photonics* 2016, **10**: 611–616.

[8] Chen J, You D, Zhang Y, *et al*. Highly sensitive and tunable self-powered UV photodetectors driven jointly by p–n junction and ferroelectric polarization. *ACS Appl Mater Interfaces* 2020, **12**: 53957–53965.

[9] Zhong HY, Xiao HY, Jiao N, *et al*. Boosting piezoelectric response of KNN-based ceramics with strong visible-light absorption. *J Am Ceram Soc* 2019, **102**: 6422–6426.

[10] Pandey SK, James AR, Raman R, *et al*. Structural, ferroelectric and optical properties of PZT thin films. *Physica B* 2005, **369**: 135–142.

[11] Mukherjee S, Phuyal D, Segre CU, *et al*. Structure and electronic effects from Mn and Nb co-doping for low band gap $BaTiO_3$ ferroelectrics. *J Phys Chem C* 2021, **125**: 14910–14923.

[12] Pei WJ, Chen J, You D, *et al*. Enhanced photovoltaic effect in Ca and Mn co-doped $BiFeO_3$ epitaxial thin films. *Appl Surf Sci* 2020, **530**: 147194.

[13] Chen J, Wang ZH, He HF, *et al*. High-performance self-powered ultraviolet photodetector based on coupled ferroelectric depolarization field and heterojunction built-in potential. *Adv Electron Mater* 2021, **7**: 2100717.

[14] Grinberg I, West DV, Torres M, *et al*. Perovskite oxides for visible-light-absorbing ferroelectric and photovoltaic materials. *Nature* 2013, **503**: 509–512.

[15] Chen J, Pei WJ, Chen G, *et al*. Greatly enhanced photocurrent in inorganic perovskite $[KNbO_3]_{0.9}$

$[BaNi_{0.5}Nb_{0.5}O_{3-\sigma}]_{0.1}$ ferroelectric thin-film solar cell. *J Am Ceram Soc* 2018, **101**: 4892–4898.

[16] Nechache R, Harnagea C, Li S, *et al*. Bandgap tuning of multiferroic oxide solar cells. *Nat Photonics* 2015, **9**: 61–67.

[17] Tang WB, Zhang YJ, Yuan CL, *et al*. Crystal structures and electrical properties of Sr/Fe-modified $KNbO_3$ ferroelectric semiconductors with narrow bandgap. *J Am Ceram Soc* 2021, **104**: 2181–2190.

[18] Wu LY, Podpirka A, Spanier JE, *et al*. Ferroelectric, optical, and photovoltaic properties of morphotropic phase boundary compositions in the $PbTiO_3$–$BiFeO_3$–$Bi(Ni_{1/2}Ti_{1/2})O_3$ system. *Chem Mater* 2019, **31**: 4184–4194.

[19] Saito Y, Takao H, Tani T, *et al*. Lead-free piezoceramics. *Nature* 2004, **432**: 84–87.

[20] Guo JM, Xu F, Shang XZ, *et al*. High-performance small-amount Fe_2O_3-doped $(K,Na)NbO_3$-based lead-free piezoceramics with irregular phase evolution. *J Am Ceram Soc* 2016, **99**: 2341–2346.

[21] Alkathy MS, Lente MH, Eiras JA. Bandgap narrowing of $Ba_{0.92}Na_{0.04}Bi_{0.04}TiO_3$ ferroelectric ceramics by transition metals doping for photovoltaic applications. *Mater Chem Phys* 2021, **257**: 123791.

[22] Shang XZ, Guo JM, Xiao WP, *et al*. The effects of Ta substitution and K/Na ratio variation on the microstructure and properties of $(K,Na)NbO_3$-based lead free piezoelectric ceramics. *J Electron Mater* 2014, **43**: 1424–1431.

[23] Xu F, Chen J, Lu YM, *et al*. Exploration on the origin of enhanced piezoelectric properties in transition-metal ion doped KNN based lead-free ceramics. *Ceram Int* 2018, **44**: 16745–16750.

[24] Zhang QF, Xu F, Yang R, *et al*. Suppressed $\tan\delta$ and enhanced Q_m in KCT and Ni_2O_3 co-modified $[(K_{0.43}Na_{0.57})_{0.94}Li_{0.06}][(Nb_{0.94}Sb_{0.06})_{0.95}Ta_{0.05}O_3]$ lead-free piezoelectric ceramics. *Ceram Int* 2017, **43**: 2537–2540.

[25] Bomlai P, Sinsap P, Muensit S, *et al*. Effect of MnO on the phase development, microstructures, and dielectric properties of $0.95Na_{0.5}K_{0.5}NbO_3$–$0.05LiTaO_3$ Ceramics. *J Am Ceram Soc* 2008, **91**: 624–627.

[26] Zhang BP, Zhang LM, Li JF, *et al*. Effect of sintering temperature on electrical properties of $Na_{0.5}K_{0.5}NbO_3$ lead-free piezoelectric ceramics prepared by normal sintering. *Ferroelectrics* 2007, **358**: 188–195.

[27] Shannon RD. Revised effective ionic radii and systematic studies of interatomic distances in halides and chalcogenides. *Acta Crystallogr A* 1976, **A32**: 751–767.

[28] Huan Y, Wang XH, Li LT. Displacement of Ta-O bonds near polymorphic phase transition in Li-, Ta-, and Sb-modified $(K,Na)NbO_3$ ceramics. *Appl Phys Lett* 2014, **104**: 242905.

[29] Li P, Li W, Zhai JW, *et al*. Composition dependence of phase structure and electrical properties of $BiMnO_3$-modified $Bi_{0.5}(Na_{0.8}K_{0.2})_{0.5}TiO_3$ thin films. *RSC Adv* 2015, **5**: 62713–62718.

[30] Hu QB, Du HW, Feng W, *et al*. Studying the roles of Cu and

Sb in $K_{0.48}Na_{0.52}NbO_3$ lead-free piezoelectric ceramics. *J Alloys Compd* 2015, **640**: 327–334.

[31] López R, Gómez R. Band-gap energy estimation from diffuse reflectance measurements on sol–gel and commercial TiO_2: A comparative study. *J Sol–gel Sci Techn* 2012, **61**: 1–7.

[32] Hong Y, Li J, Wu WJ, *et al*. Structure, electricity, and bandgap modulation in Fe_2O_3-doped potassium sodium niobate ceramics. *Ceram Int* 2018, **44**: 16069–16075.

[33] Balberg I, Pinch HL. The optical absorption of iron oxides. *J Magn Magn Mater* 1978, **7**: 12–15.

[34] Xiao HY, Dong W, Guo YP, *et al*. Design for highly piezoelectric and visible/near-infrared photoresponsive perovskite oxides. *Adv Mater* 2019, **31**: 1805802.

[35] Huangfu G, Xiao HY, Guan L, *et al*. Visible or near-infrared light self-powered photodetectors based on transparent ferroelectric ceramics. *ACS Appl Mater Interfaces* 2020, **12**: 33950–33959.

[36] Xiao HY, Luo CT, Huangfu G, *et al*. Boosting the photocatalytic ability of bandgap engineered $(Na_{0.5}Bi_{0.5})TiO_3$–$BaTiO_3$ by N–Ni codoping. *J Phys Chem C* 2020, **124**: 11810–11818.

[37] Chakrabartty JP, Nechache R, Harnagea C, *et al*. Photovoltaic effect in multiphase Bi–Mn–O thin films. *Opt Express* 2014, **22**: A80–A89.

[38] Liu FM, Fina I, Gutiérrez D, *et al*. Selecting steady and transient photocurrent response in $BaTiO_3$ films. *Adv Electron Mater* 2015, **1**: 1500171.

[39] Yi HT, Choi T, Choi SG, *et al*. Mechanism of the switchable photovoltaic effect in ferroelectric $BiFeO_3$. *Adv Mater* 2011, **23**: 3403–3407.

[40] He HC, He ZL, Jiang ZL, *et al*. A controllable photoresponse and photovoltaic performance in $Bi_4Ti_3O_{12}$ ferroelectric thin films. *J Alloys Compd* 2017, **694**: 998–1003.

[41] Si SF, Deng HM, Zhou WL, *et al*. Modified structure and optical band-gap in perovskite ferroelectric $(1-x)$ $KNbO_3$–$x$$BaCo_{1/3}Nb_{2/3}O_3$ ceramics. *Ceram Int* 2018, **44**: 14638–14644.

[42] Pal S, Swain AB, Biswas PP, *et al*. Giant photovoltaic response in band engineered ferroelectric perovskite. *Sci Rep* 2018, **8**: 8005.

[43] Machado P, Scigaj M, Gazquez J, *et al*. Band gap tuning of solution-processed ferroelectric perovskite $BiFe_{1−x}Co_xO_3$ thin films. *Chem Mater* 2019, **31**: 947–954.

[44] Sun YZ, Guo F, Chen JY, *et al*. Improved ferroelectric and photovoltaic properties of $BiMnO_3$ modified lead-free $K_{0.5}Na_{0.5}NbO_3$ solid-solution films. *Appl Phys Lett* 2017, **111**: 253901.

[45] Wang XW, Sun LY, Wang XE, *et al*. A facile hot plate annealing at low temperature of $Pb(Zr_{0.52}Ti_{0.48})O_3$ thin films by sol–gel method and their ferroelectric properties. *J Mater Sci-Mater El* 2018, **29**: 5660–5667.

[46] Han H, Kim D, Chae SM, *et al*. Switchable ferroelectric photovoltaic effects in epitaxial h-RFeO$_3$ thin films.

Nanoscale 2018, **10**: 13261–13269.

[47] Wu M, Lou XJ, Li TY, *et al*. Ni-doped $SrBi_2Nb_2O_9$— Perovskite oxides with reduced band gap and stable ferroelectricity for photovoltaic applications. *J Alloys Compd* 2017, **724**: 1093–1100.

[48] Zhang GH, Wu H, Li GB, *et al*. New high T_C multiferroics $KBiFe_2O_5$ with narrow band gap and promising photovoltaic effect. *Sci Rep* 2013, **3**: 1265.

[49] Sun YZ, Guo F, Lu QS, *et al*. Improved ferroelectric photovoltaic effect in Mn-doped lead-free $K_{0.5}Na_{0.5}NbO_3$ films. *Ceram Int* 2018, **44**: 13994–13998.

[50] Kumari S, Ortega N, Pradhan DK, *et al*. Effect of thickness on dielectric, ferroelectric, and optical properties of Ni substituted $Pb(Zr_{0.2}Ti_{0.8})O_3$ thin films. *J Appl Phys* 2015, **118**: 184103.

[51] Bai YL, Chen JY, Wu X, *et al*. Photovoltaic behaviors regulated by band-gap and bipolar electrical cycling in holmium-doped $Bi_5Ti_3FeO_{15}$ ferroelectric films. *J Phys Chem C* 2016, **120**: 24637–24645.

[52] An H, Han JY, Kim B, *et al*. Large enhancement of the photovoltaic effect in ferroelectric complex oxides through bandgap reduction. *Sci Rep* 2016, **6**: 28313.

[53] Liu H, Chen J, Ren Y, *et al*. Large photovoltage and controllable photovoltaic effect in $PbTiO_3$–$Bi(Ni_{2/3+x}Nb_{1/3−x})O_{3−δ}$ ferroelectrics. *Adv Electron Mater* 2015, **1**: 1400051.

[54] Pan WY, Tang YC, Yin Y, *et al*. Ferroelectric and photovoltaic properties of $(Ba,Ca)(Ti,Sn,Zr)O_3$ perovskite ceramics. *Ceram Int* 2021, **47**: 23453–23462.

[55] Lan YC, Tang WB, Yuan CL, *et al*. Achieving ultrahigh photocurrent density of Mg/Mn-modified $KNbO_3$ ferroelectric semiconductors by bandgap engineering and polarization maintenance. *Chem Mater* 2022, **34**: 4274–4285.

[56] Han F, Zhang YJ, Yuan CL, *et al*. Photocurrent and dielectric/ferroelectric properties of $KNbO_3$–$BaFeO_{3−δ}$ ferroelectric semiconductors. *Ceram Int* 2020, **46**: 14567–14572.